

UC San Diego

UC San Diego Previously Published Works

Title

The California Undercurrent as a Source of Upwelled Waters in a Coastal Filament

Permalink

<https://escholarship.org/uc/item/58r8t0ws>

Journal

Journal of Geophysical Research - Oceans, 126(2)

ISSN

2169-9275

Authors

Zaba, Katherine D

Franks, Peter JS

Ohman, Mark D

Publication Date




2021-02-01

DOI

10.1029/2020jc016602

Peer reviewed

The California Undercurrent as a Source of Upwelled Waters in a Coastal Filament

 Katherine D. Zaba¹ , Peter J. S. Franks¹ , and Mark D. Ohman¹ 
¹Scripps Institution of Oceanography, La Jolla, CA, USA

Key Points:

- Cross-shore filament transports water from coastal margin to open ocean
- Water mass composition within core of filament's jet is heterogeneous
- Recently upwelled California Undercurrent water corresponds with higher chlorophyll-*a* fluorescence than California Current water

Supporting Information:

- Supporting Information S1
- Figure S1
- Figure S2
- Figure S3
- Figure S4
- Figure S5
- Figure S6
- Figure S7
- Figure S8

Correspondence to:

 K. D. Zaba,
kzaba@ucsd.edu

Citation:

 Zaba, K. D., Franks, P. J. S., & Ohman, M. D. (2021). The California Undercurrent as a source of upwelled waters in a coastal filament. *Journal of Geophysical Research: Oceans*, 126, e2020JC016602. <https://doi.org/10.1029/2020JC016602>

 Received 15 JUL 2020
 Accepted 19 JAN 2021

Abstract In the California Current System, cross-shore transport of upwelled, nutrient-rich waters from the coastal margin to the open ocean can occur within intermittent, submesoscale-to-mesoscale features such as filaments. Time-varying spatial gradients within filaments affect net cross-shore fluxes of physical, biological, and chemical tracers but require high-resolution measurements to accurately estimate. In June 2017, the *California Current Ecosystem* Long Term Ecological Research program process cruise (P1706) conducted repeat sections by an autonomous *Spray* glider and a towed SeaSoar to investigate the role of one such coastal upwelling feature, the Morro Bay filament, which was characterized by enhanced cross-filament gradients (both physical and biological) and an along-filament jet. Within the jet, speeds were up to 0.78 m/s and the offshore transport was 1.5 Sverdrups (3.8 Sverdrups) in the upper 100 m (500 m). A climatological data product from the sustained California Underwater Glider Network provided necessary information for water mass differentiation. The analysis revealed that the cold, salty side of the filament carried recently upwelled California Undercurrent water and corresponded to higher chlorophyll-*a* fluorescence than the warm, fresh side, which carried California Current water. Thus, there was a convergence of heterogeneous water masses within the core of the filament's offshore-flowing jet. These water masses have different geographic origins and thermohaline characteristics, which has implications for filament-related cross-shore fluxes and submesoscale-to-mesoscale biological community structure gradients.

Plain Language Summary In the California Current System, slow broad currents move water in the alongshore direction but fast narrow flow features, such as filaments, can move water from the coast to the open ocean. Water at the coast tends to be cold, dense, and nutrient-rich, thus filaments serve as an important mechanism for biogeochemical supply to nutrient-poor offshore waters. In June 2017, an oceanographic experiment was conducted to measure a filament off the coast of Morro Bay, California. This study presents results from that experiment, specifically data from an autonomous underwater glider, *Spray*, and a ship-towed platform, SeaSoar. The high-resolution measurements reveal that there was a confluence of warm, fresh and cold, salty water within the filament, which originated far offshore and at the coast, respectively. The cold, salty side corresponded to more phytoplankton.

1. Introduction

Coastal wind-driven upwelling is a key mechanism supplying nutrients to the euphotic zone and driving biological productivity in the California Current System (CCS) (Rykczewski & Checkley, 2008). Upwelling is highly variable in space and time (Jacox et al., 2018), as is the subsequent cross-shore and alongshore horizontal transport of nutrient-rich, upwelled waters. The three-dimensional transport mechanisms and pathways of coastally upwelled water are complex, leading to patchy biological growth and export, and heterogeneous ecosystem conditions throughout the CCS. In this study, we describe the physical and biological gradients associated with one such pathway: a cross-shore coastal upwelling filament observed offshore of Morro Bay, CA during June 2017. High-resolution measurements from an intensive process study reveal that there was a confluence of two distinct water masses at the sampled filament: recently upwelled California Undercurrent water and California Current water from offshore. There was a local maximum in biological production coincident with the California Undercurrent water.

Water masses of distinct origins (subarctic, subtropical, tropical) meet in the southern CCS (Bograd et al., 2019), resulting in strong lateral gradients of temperature, salinity, oxygen, nutrient concentration

(Hickey 1979), and, consequently, species distribution and total community biomass (Kenitz et al., 2019). Mean alongshore circulation of the southern CCS is composed of the equatorward California Current (CC) and poleward California Undercurrent (CU). The CC is a broad, slow, meandering (Centurioni et al., 2008) surface current that is located offshore (Rudnick et al., 2017), transporting cold, fresh Pacific Subarctic water (Lynn & Simpson, 1987) from the north into the midlatitude CCS domain. The CU is a narrow current, approximately 100–150 km in cross-shore width (Rudnick et al., 2017; Zaba et al., 2018), with a vast meridional extent of contiguous flow along the North American coast (Pierce et al., 2000; Thomson & Krassovski, 2010). It carries warm, salty Equatorial Pacific water of tropical southerly origin (Lynn & Simpson, 1987) into the midlatitudes. While the CU core is subsurface, centered approximately on the 26.0 kg/m³ isopycnal (~100 m depth), the term “undercurrent” may be a misnomer in the southern CCS domain, as the poleward flow often extends from at least 500 m depth to the surface, especially during its semiannual intensification in winter and summer (Gomez-Valdivia et al., 2017; Rudnick et al., 2017; Zaba et al., 2018). Due to its proximity to the coast and the ocean surface, CU water is a dominant source for coastal upwelling (Hickey & Banas 2003; Lynn & Simpson, 1987). In the mean cross-shore upwelling overturning cell (Davis, 2010), CU water flows upward at the coast and offshore in a thin Ekman layer (Chereskin, 1995; Zaba et al., 2020). There is great interest in determining the source depth and properties of upwelled water, as well as cross-shore fluxes associated with westward propagating circulation, due to their implications for coastal heat and nutrient budgets.

Beyond the low-frequency statistical view, the instantaneous CCS flow field is dominated by submesoscale to mesoscale features such as eddies, filaments, meanders, and jets that deform the mean flow (Chereskin et al., 2000; Davis, 1985). These features are relevant for horizontal transport, with filaments providing one particular mechanism for the cross-shore transport of upwelled water. The Coastal Transition Zone (CTZ) program of 1987–1988 aimed to understand the dynamics and implications of filaments, which were defined as narrow (<100 km) “cold surface features” that originate near the coast and extend offshore (Brink & Cowles, 1991) in eastern boundary current regions. Strub et al. (1991) attributed the flow structure of cold filaments to three possible conceptual models: one-way offshore-flowing “squirts,” the outside edges of cyclonic and anticyclonic vortices in a mesoscale eddy field, and the boundaries between a meandering southward jet and a cyclonic cold core eddy. The main filament surveyed in the central CCS during the CTZ experiments was determined to be the latter (Strub et al., 1991); all surveyed CTZ filaments had a sharp temperature and salinity front and an offshore-flowing jet that acted as a boundary separating water masses (Huyer et al., 1991), as well as phytoplankton and zooplankton species (Hood et al., 1990, 1991; Mackas et al., 1991). Further poleward in the northern CCS off Oregon, the US Global Ocean Ecosystem Dynamics Northeast Pacific program focused in part on observing cross-shore filaments, revealing a correspondence between filaments’ cold upwelled waters, an elevated phytoplankton biomass (Barth et al., 2005), and an abundance of coastal zooplankton taxa (Keister, Cowles, et al., 2009; Keister, Peterson, et al., 2009). Sustained *Spray* glider measurements in the southern CCS show that phytoplankton and zooplankton gradients are generally enhanced at frontal boundaries (McClatchie et al., 2012; Powell & Ohman, 2015), whether those fronts are related to filaments or otherwise.

Here we readdress some of the same questions asked about filaments’ physical and biological structure during previous experiments: what is a typical filament cross section of temperature, salinity, density, velocity, plankton? Where does a filament’s water come from? Where does it go? Is there net offshore transport associated with such features? However, we apply new observing technologies developed over the last 30 years, including autonomous sensing platforms, and an improved high-resolution baseline of regional circulation patterns and water masses from sustained observations in the California Underwater Glider Network (CUGN) (Rudnick et al., 2017). The *California Current Ecosystem*–Long Term Ecological Research (CCE-LTER) program (Ohman et al., 2013) conducted an extensive process study of a filament during June–July 2017 (Figure 1), hereafter referred to as the P1706 study and the Morro Bay filament. This manuscript presents hydrographic and chlorophyll-*a* fluorescence measurements from *Spray* glider and towed SeaSoar surveys; the measurements are interpreted in the context of the independent CUGN climatology. Other CCE-LTER team members are working on addressing the biogeochemical consequences of the Morro Bay filament from a series of Lagrangian measurements made during P1706. The remainder of this paper is organized as follows: Sections 2.1, 2.2 describe the *Spray* glider and SeaSoar observations, 2.3 the objective mapping methodology applied to both datasets, and 2.4 the application of the CUGN climatology for water

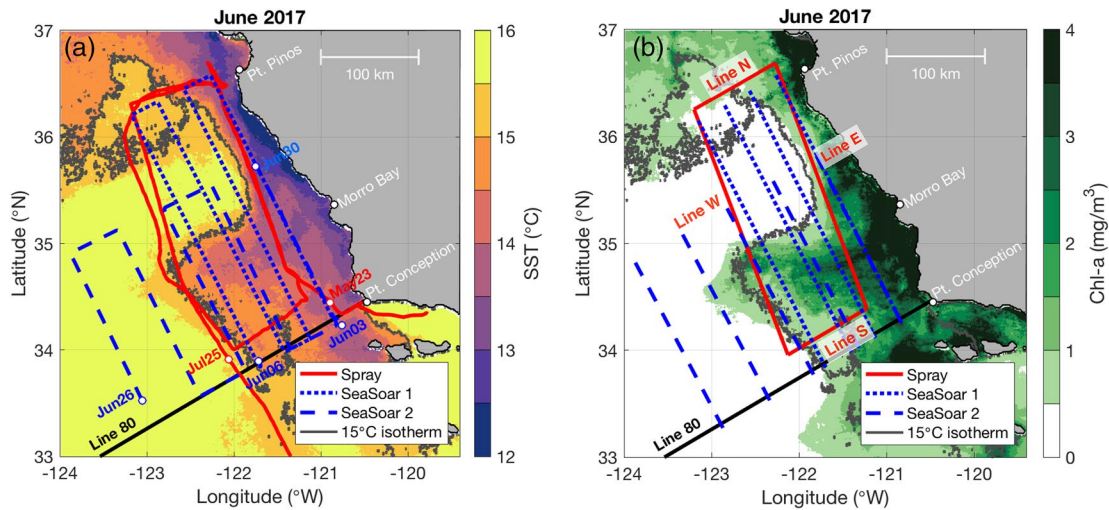


Figure 1. Plan view of mean June 2017 satellite-derived (a) sea surface temperature and (b) surface chlorophyll-*a* concentration. (a) Spray glider mission (red solid line), SeaSoar surveys 1 (blue dotted line) and 2 (blue dashed line), with relevant survey start and end dates marked with white dots and labeled: 23 May–25 Jul (Spray), 3–6 Jun (SeaSoar 1), 26–30 Jun (SeaSoar 2). (b) Longitude-latitude grids to which the datasets are objectively mapped, with the glider perimeter sections labeled Lines N, S, E, W. Both panels include the 15°C isotherm (dark gray contour), CalCOFI line 80 (black solid line) and a horizontal distance scale bar (upper right corner).

mass differentiation; Section 3 presents and discusses the hydrography of the filament (3.1, 3.2) and its consequences for patchy biological productivity (3.3); Section 4 summarizes the results and discusses their implications.

2. Data and Methods

2.1. Spray Glider

The *Spray* glider (Sherman et al., 2001) is a buoyancy-driven autonomous underwater vehicle that vertically profiles the ocean in a sawtooth pattern from the surface to a specified depth, in this case 500 m. The platform carried a suite of sensors, including a Seabird conductivity-temperature-depth sensor (CTD), Sontek acoustic Doppler profiler (ADP), Seapoint chlorophyll fluorometer, and in situ ultraviolet spectrophotometer (ISUS) optical nitrate sensor. The ISUS sensor on the *Spray* malfunctioned during P1706, so nitrate measurements were not obtained. During the ascent of each dive cycle, depth-dependent profiles of the following variables were sampled at 1/8 Hz: pressure, temperature, conductivity, water velocity, acoustic backscatter, and Chl-*a* fluorescence. Depth-averaged velocity over 0–500 m is calculated from dead-reckoning between glider GPS fixes at the ocean surface (Rudnick et al., 2018). The glider moves relatively slowly through the water, with a horizontal speed of approximately 25 cm/s and a vertical speed of 10 cm/s. In this configuration, spacing of profiles is approximately 3 km in horizontal distance and 3 h in time. Data are vertically block averaged to 10 m depth bins. During P1706, the glider was piloted along a rectangular perimeter in a counterclockwise direction over May 23–July 25, 2017 (Figure 1a). The box perimeter extended meridionally from Pt. Conception to Pt. Piños (southern end of Monterey Bay). The full mission started offshore of Goleta, CA on 18 May 2017 and ended offshore of San Diego, CA on 24 August 2017.

2.2. SeaSoar

The SeaSoar (Pollard, 1986) is a ship-towed platform that moves at the horizontal speed of the vessel (here ~8 knots or 4 m/s) and undulates vertically in a sawtooth pattern, providing a more synoptic survey of the upper ocean than the slower-moving glider. Two SeaSoar surveys were conducted between Pt. Conception and Pt. Piños (Figure 1a), spanning the site where the Morro Bay coastal upwelling filament had been detected in satellite imagery as low SST (Figure 1a) and high Chl-*a* (Figure 1b). Four cross-filament/along-shore transect lines of 293 km length and separated by 31 km in the cross-shore direction were completed

during SeaSoar survey 1 over June 3–6, 2017, and five transect lines of 191 km length and separated by 54 km during SeaSoar survey 2 over June 26–29, 2017 (Figure 1a). The deployment protocols for the SeaSoar required a minimum bottom depth of 500 m, which precluded sampling very close to the coast at the point of origin of the upwelling filament. The SeaSoar cycled between the surface and approximately 250 m depth. It was equipped with dual CTDs, a Chl-*a* fluorometer, dissolved oxygen sensor, and beam transmissometer. Data from only one of the CTDs are used in this analysis because of consistent conductivity cell performance throughout. The temperature and conductivity data were sampled at 24 Hz. Following the calibration method of Ferrari and Rudnick (2000), salinity spiking is reduced by applying phase lag corrections to the 24 Hz conductivity and temperature data. The despiked 24 Hz data are block averaged to 1 Hz, then binned to two-dimensional, along-ship track sections of 5 m vertical and 9 min temporal resolution.

2.3. Objective Mapping

The primary purposes of objectively mapping the *Spray* and SeaSoar data (Figure 1a) are to (1) interpolate the data onto straight, uniformly gridded sections (Figure 1b), which facilitates subsequent calculations, and (2) remove the variability associated with internal waves and other high-frequency oceanic processes. Here the objective maps are one dimensional in along-track horizontal distance, calculated discretely at each depth bin. A Gaussian covariance is assumed, with a horizontal decorrelation length scale of 15 km, as well as a noise-to-signal ratio of 0.1. The result is gridded sections (Figure 1b) with 5 km along-track by 10 m vertical resolution for *Spray* data and 5 m for SeaSoar data, calculated for temperature, salinity, and velocity. Other variables such as potential density and geostrophic velocity are derived from the mapped fields. Normalized mean squared error (MSE) is also a product of the objective mapping algorithm, where error increases with increasing distance between grid points and data locations. In this analysis, maps are masked where MSE is greater than 0.3.

2.4. Water Mass Differentiation

The CUGN climatology (Rudnick et al., 2017) provides a baseline for subsurface water mass definitions and differentiation based on potential temperature, salinity, and velocity characteristics. There are several data products along three CalCOFI lines (66.7, 80, 90) included in the CUGN climatology. In this analysis, we use the high-resolution (10 m vertical by 5 km horizontal) mean data product along CalCOFI line 80, which is calculated over years 2007–2013 (inclusive). Line 80 begins at Point Conception and extends offshore, oriented roughly perpendicular to the coast; it is located at the southern end of the P1706 study site (Figure 1a). Mean alongshore velocity across line 80 (Figure 2a and 2b) is composed of: the poleward CU spanning 0–115 km from shore with a subsurface velocity core, and the surface-intensified, equatorward CC occupying the remaining offshore portion of the section. The water masses carried by the CU and CC have different origins and thermohaline structures, thus they separate out distinctly in θ - S space (Figure 2c). According to Lynn and Simpson (1987), cold, fresh Pacific Subarctic water constitutes the salinity minimum of the CC, whereas warm, salty Equatorial Pacific water constitutes the salty core of the CU and is a source for coastal upwelling. Isobar, isopycnal, and isotherm salinity is greater in the poleward CU than the equatorward CC (Figure 2b and 2c). Several P1706 transects (Figure 1a) were located at the climatological boundary between the CU and CC, and were thus well-suited for assessing cross-shore exchange of these two water masses.

Mean line 80 alongshore circulation and cross-shore thermohaline structure from the CUGN climatology (Figure 2) inform CCS water mass definitions for this study. We define the CU-CC boundary as the zero-crossing of the 0–500 m depth-averaged alongshore velocity, which is located approximately 115 km offshore along line 80 (Figure 2a). We set a 40-km buffer on either side of this boundary, such that the offshore bound for the CU water mass is 75 km from shore and the inshore bound for the CC water mass is 155 km from shore. The 40-km buffer is chosen based on the following criteria: (1) it is longer than the horizontal decorrelation length scale of 30 km used to calculate the CUGN climatology (Rudnick et al., 2017) and (2) it is short enough to exclude the CU velocity core from the buffer zone (the CU velocity core should be within the CU water mass boundary). Transformed into θ - S space, these boundaries represent the lower limit for CU salinity and the upper limit for CC salinity (Figure 2b), respectively. Water parcels occupying the θ - S

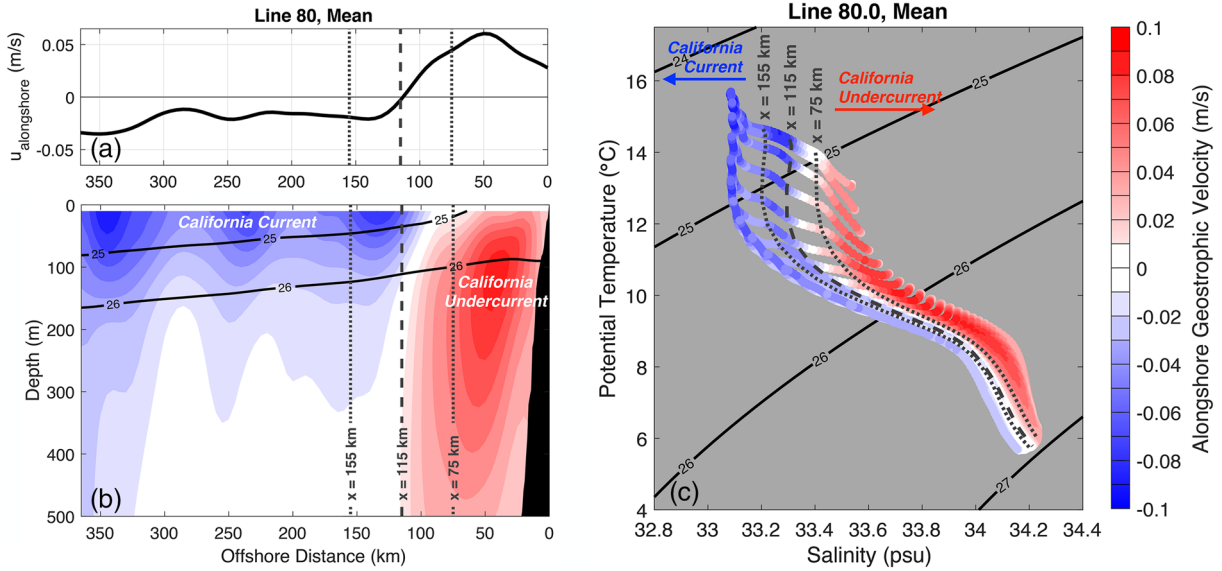


Figure 2. Mean alongshore (a) 0–500m depth-averaged velocity, $u_{\text{alongshore}}$, and (b and c) depth-dependent geostrophic velocity across CUGN line 80.0 as a function of offshore distance in panel (a and b) and θ -S in panel (c). In all panels, positive (red) is poleward flow and negative (blue) is equatorward; the dashed gray line at $x = 115$ km is the CU-CC boundary, defined as the location of the zero crossing of $u_{\text{alongshore}}$ in panel (a); the dotted gray lines at $x = 75$ km and 155 km are ± 40 km the CU-CC boundary location. In physical space (a and b), the dotted lines are the inshore and offshore boundaries of the CC and CU, respectively. In θ -S space (c), the dotted lines are the upper and lower salinity boundaries of the CC and CU, respectively. Solid black labeled contours are isopycnals in (b and c).

space saltier than the $x = 75$ km θ -S profile in Figure 2b denote CU water. Likewise, water parcels occupying the θ -S space fresher than the $x = 155$ km θ -S profile in Figure 2b denote CC water. Water parcels in the buffer zone between $x = 75$ km and $x = 155$ km represent a mixture of CC and CU water, however, there will be no fractional estimate of water type based on linear mixing and those water parcels will remain unclassified, denoted “neither” or “other.” To summarize, we are using the high-resolution mean data product from the CUGN climatology to define the fresh CC and salty CU water masses in physical and θ -S spaces. Subsequently in this manuscript, we will apply these water mass definitions to interpret the Morro Bay filament of P1706. In other words, a long-term statistical view of alongshore circulation will inform an event view of cross-shore transport during this process study.

2.5. Vertically Integrated Parameters

Here we define several vertically integrated parameters that will be repeatedly referred to throughout the manuscript. These parameters are calculated from the objectively mapped data, which are uniformly gridded in horizontal distance and depth, as explained in Section 2.3, facilitating summations over a range of discrete depth bins.

Applying the water mass differentiation of Section 2.4 to objectively mapped data yields gridded sections of 5 km by 10 m bins that are tagged as CU water, CC water, or neither. For any given along-section profile, we can calculate the percentage of CU (%CU) and CC (%CC) waters over a given depth range by the following summations:

$$\%CU_{z_1:z_2} = \frac{100}{z_2 - z_1} \sum_{k=z_1}^{z_2} h_k C_k, \text{ where } C_i = \begin{cases} 1, & \text{if CU water type} \\ 0, & \text{otherwise} \end{cases}$$

$$\%CC_{z_1:z_2} = \frac{100}{z_2 - z_1} \sum_{k=z_1}^{z_2} h_k C_k, \text{ where } C_i = \begin{cases} 1, & \text{if CC water type} \\ 0, & \text{otherwise} \end{cases}$$

where z_1 and z_2 are depth values ($z_i \geq 0$ and $z_1 < z_2$), h_k is the depth bin height, and C_k is a Boolean variable that is 1 if the water type in the depth bin matches that of the calculation and 0 otherwise. If the θ -S characteristics of the water type in a given depth bin fall within the buffer zone between CU and CC boundaries (Figure 2c), the water mass type is “other,” and the C_k value is 0. The sum of %CU and %CC does not necessarily have to equal 100% because a depth bin may have other water types present or a nondistinct mix of CU and CC water types.

Vertically integrated Chl-*a* fluorescence will be calculated as:

$$F_{z_1:z_2} = \frac{1}{z_2 - z_1} \sum_{k=z_1}^{z_2} h_k F_k$$

where F_k is the in situ fluorometer reading for a discrete depth bin in units of *volts* and $F_{z_1:z_2}$ is Chl-*a* fluorescence integrated over the depth range z_1 to z_2 in units of *volts*. The relationships between %CU $_{z_1:z_2}$, %CC $_{z_1:z_2}$, and $F_{z_1:z_2}$ will be examined.

3. Results and Discussion

3.1. Hydrography of the CU

The poleward CU was present in all three cross-shore sections made by the glider during P1706. The along-shore transports across Line N and Line S of Lap 1 and Line N of Lap 2 (Figure S1b, S1d, and S1f) were 3.1, 3.7, and 3.3 Sv, respectively, where positive is poleward. Similar to the CUGN mean (Figure 2a), the depth-averaged alongshore velocity during P1706 had a parabolic cross-shore structure with a maximum in poleward flow near the climatological location of the CU velocity core, and decreasing poleward flow toward the west (offshore). During the Line E transect of glider lap 1, the strong poleward CU flow at the northeast corner of the rectangular perimeter swept the glider northwestward such that the glider had to double back against the current to return to its intended course. This overshoot is apparent in the glider track (red line) of Figure 1a. The presence of the alongshore CU during P1706 predicated the subsequent analysis of the cross-shore transport of the water mass carried by the CU.

3.2. Hydrography of the Morro Bay Filament

The Morro Bay filament was identified in satellite imagery as an offshore protrusion of cold, likely recently upwelled, coastal water (Figure 1a). It extended from Morro Bay at the coast to over 100 km offshore. A sharp SST front oriented nearly cross-shore at roughly 35°N separated the filament’s cold water from relatively warm water to its north (Figure 1a). High surface Chl-*a* concentration corresponded with cold SST values at the coast and in the filament (Figure 1b), and were roughly bound by the 15°C surface isotherm. The temporal evolution of the filament as observed from satellite from May 23 to July 25, 2017 is illustrated in Figures 3a–3d and Figure S1; the surface expression of the feature was most prominent during 07–13 June (Figure S1b and S1i) and 11–24 June (Figure 3b, Figure S1c and S1j).

A strong offshore-flowing jet over 0–500 m depth was centered roughly on 35°N (Figure 3b), and thus co-located with the sharp SST front. Minimum glider-measured 0–500 m depth-averaged cross-shore velocity at the latitudinal center of the jet was -0.18 m/s (i.e., offshore) on June 19, 2017. The offshore flowing jet was flanked by weaker onshore flow to the north and south, and the section-integrated volume transport across Line W was $+1.6$ Sv onshore. θ -S profiles along Line W reveal the presence of both CU and CC water types (Figure 3f), however, most of the CU water parcels flowed offshore within the jet, whereas most of the CC water parcels flowed onshore. There are several offshore-flowing profiles in Figure 3f that carry fresh, low-density CC water near the surface. This is our first clue that the water mass composition of the jet is mostly, but not exclusively, salty CU water. The flow field was more variable along Lap 1, Line E (Figure 3a), with no apparent offshore-flowing jet; this could be due to the earlier sampling time (23 May–4 Jun) or the nearshore sampling location (Line E), which lies closer to the coastal root of the filament. Along Line E, the glider primarily sampled CU water flowing both onshore and offshore (Figure 3e), as expected given the

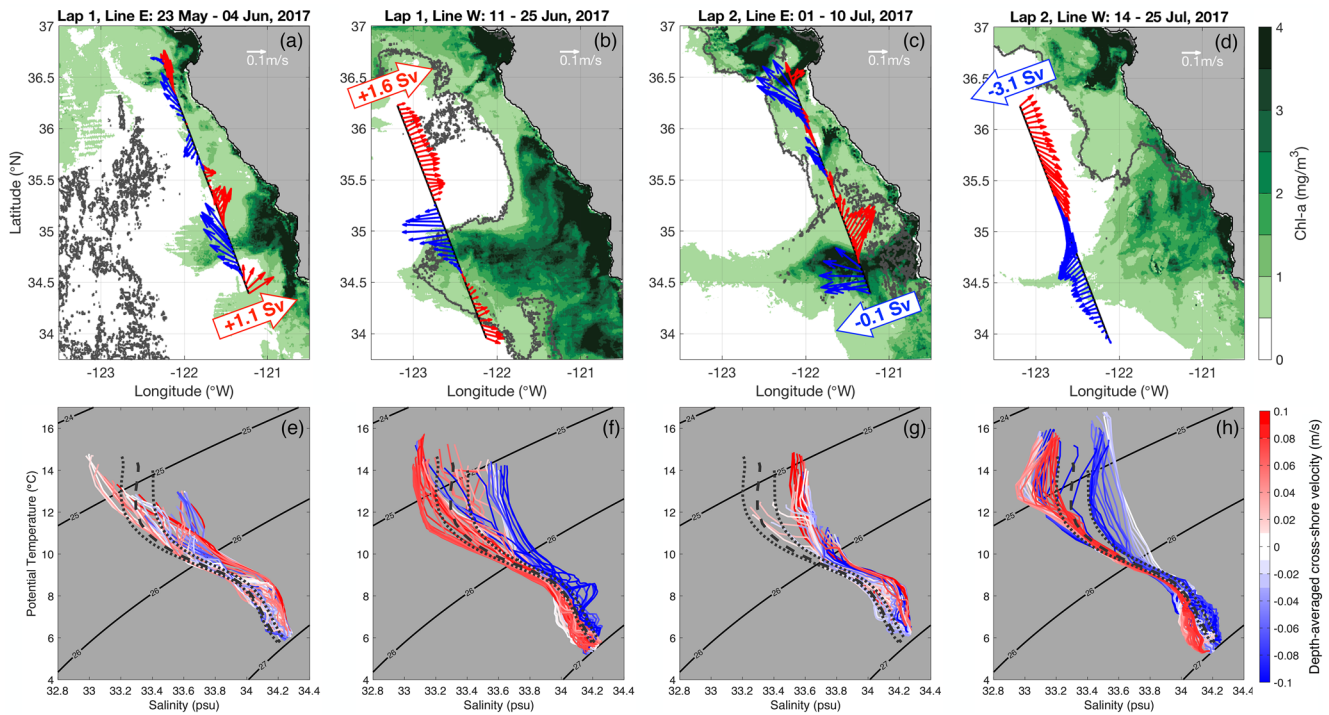


Figure 3. Circulation and water mass distribution during glider (a and e) Lap 1, Line E, (b and f) Lap 1, Line W, (c and g) Lap 2, Line E, and (d and h) Lap 2, Line W. Panels (a–d) show the satellite-derived 15°C surface isotherm (dark gray contour) and surface chlorophyll-*a* concentrations (filled contours) time-averaged over the duration of each glider section, and glider-derived objectively mapped 0–500 m depth-averaged velocities (thin arrows). The 0–500 m section integrated cross-shore volume transport values are labeled in the thick block arrows. Positive velocities and transports (red) are defined as onshore and negative (blue) as offshore. Panels (e–h) show θ -*S* profiles colored by depth-averaged cross-shore velocity to distinguish the water mass composition of distinct flow features (red is onshore, blue is offshore). CU/CC boundary (dashed gray line), CU lower bound, and CC upper bound (dotted gray lines) as defined in Figure 2 are shown for reference. CC, California Current; CU, California Undercurrent.

proximity of Line E to the CU core. A notable exception is the low-density water ($<25 \text{ kg/m}^3$), which may have been an onshore intrusion or recirculation of CC water or near-surface water influenced by air-sea or land-sea fluxes.

About a month later, during the glider's second lap about the box perimeter, horizontal circulation patterns at Line W were different (Figure 3d). Minimum depth-averaged cross-shore velocity across Line W was -0.14 m/s (78% that of the previous lap) and the swift, narrow jet was no longer present. Rather, the offshore flow during Lap 2, Line W was broader and shifted southward. The circulation was comprised of two broad flows (onshore across the northern portion of Line W and offshore across the southern) with a sense of anticyclonic vorticity—possibly an eddy circulating water across Line W. Fresh CC water flowed in both cross-shore directions, while salty CU water flowed only offshore (Figure 3h). Additional analysis (*not shown*) indicated that the water south of about 34.75°N was CU and the remaining northern part of the section was CC. Though the swift jet of Lap 1, Line W (Figure 3b) was no longer apparent, the net transport across Lap 2, Line W was -3.1 Sv , where the negative indicates offshore. As was the case during Lap 1, Line E (Figure 3a and 3e), the water sampled along Lap 2, Line E was predominantly salty CU water (Figure 3c and 3g) due to the proximity of line E to the nearshore CU core.

The focus will now be on glider Lap1, Line W (11–25 Jun) (Figure 3b and 3f), when the offshore-flowing filament extended from the surface to at least 500 m depth (Figure 4b). Its velocity profile was vertically sheared, with the fastest-moving core of the jet confined to the upper 100 m and minimum cross-shore velocities at the surface ($\sim -0.78 \text{ m/s}$), where negative indicates offshore. Over the upper 0–100 m, the filament was 50 km wide with a volume transport of -1.5 Sv (Figure 5a); over 0–500m, it was 80 km wide and transported -3.8 Sv (Figure 5b). The offshore-flowing jet was flanked on both sides by slower onshore flow (Figure 4b) such that the net volume transport across the section was positive (onshore) when in-

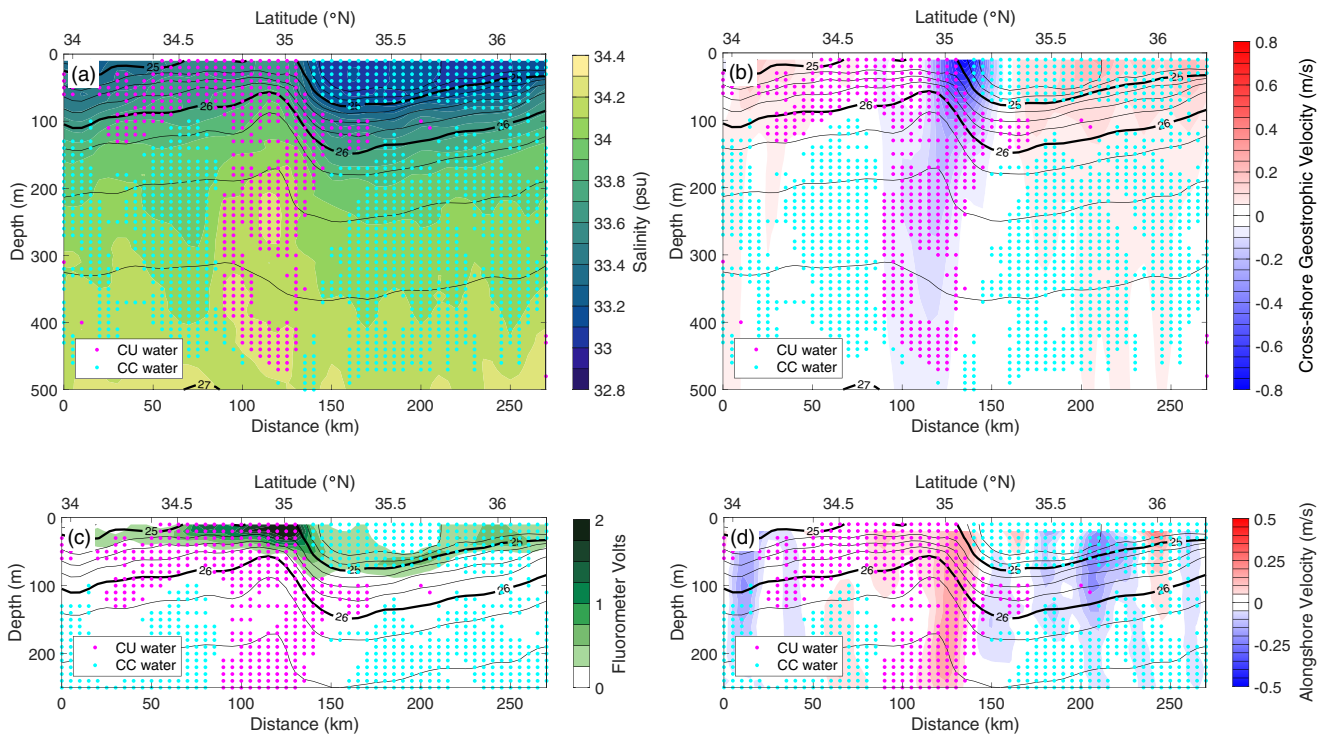


Figure 4. Depth-dependent sections along glider lap 1, line W of: (a) salinity, (b) cross-shore geostrophic velocity, (c) fluorometer volts, and (d) ADP-measured alongshore velocity. In the geostrophic velocity colormap (b), blue background shading represents offshore flow and red onshore. In the alongshore velocity colormap (d), blue background shading represents equatorward flow and red poleward. The black lines are isopycnals. The magenta dots represent CU water parcels and the cyan dots CC water parcels, the untagged bins are either a CU-CC mixture or a different water mass. ADP, acoustic Doppler profiler; CC, California Current; CU, California Undercurrent.

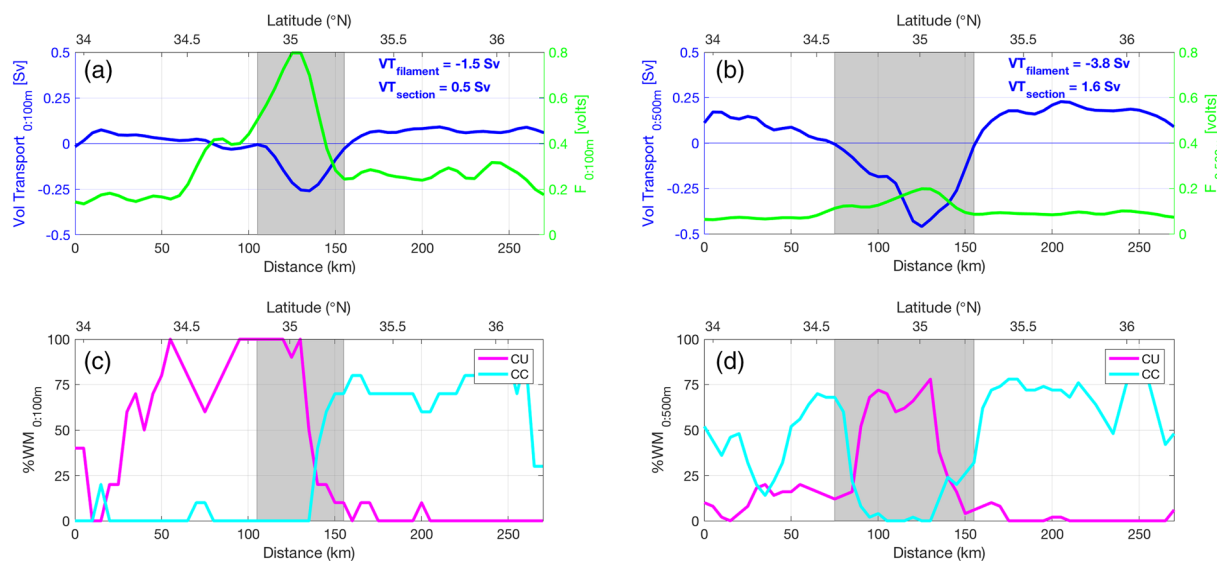


Figure 5. Glider-measured properties along lap 1, line W. (a and b) Depth-integrated cross-shore volume transport (blue) and depth-integrated fluorometer volts. (c and d) Water mass percentage of CU (magenta) and CC (cyan). Depth integrals and percentages are calculated over (a and c) 0–100 m and (b and d) 0–500 m. The location of the filament is highlighted in gray. The cross-shore volume transport integrated over the filament (VT_{filament}) and over the entire section (VT_{section}) are reported in blue text in (a and b).

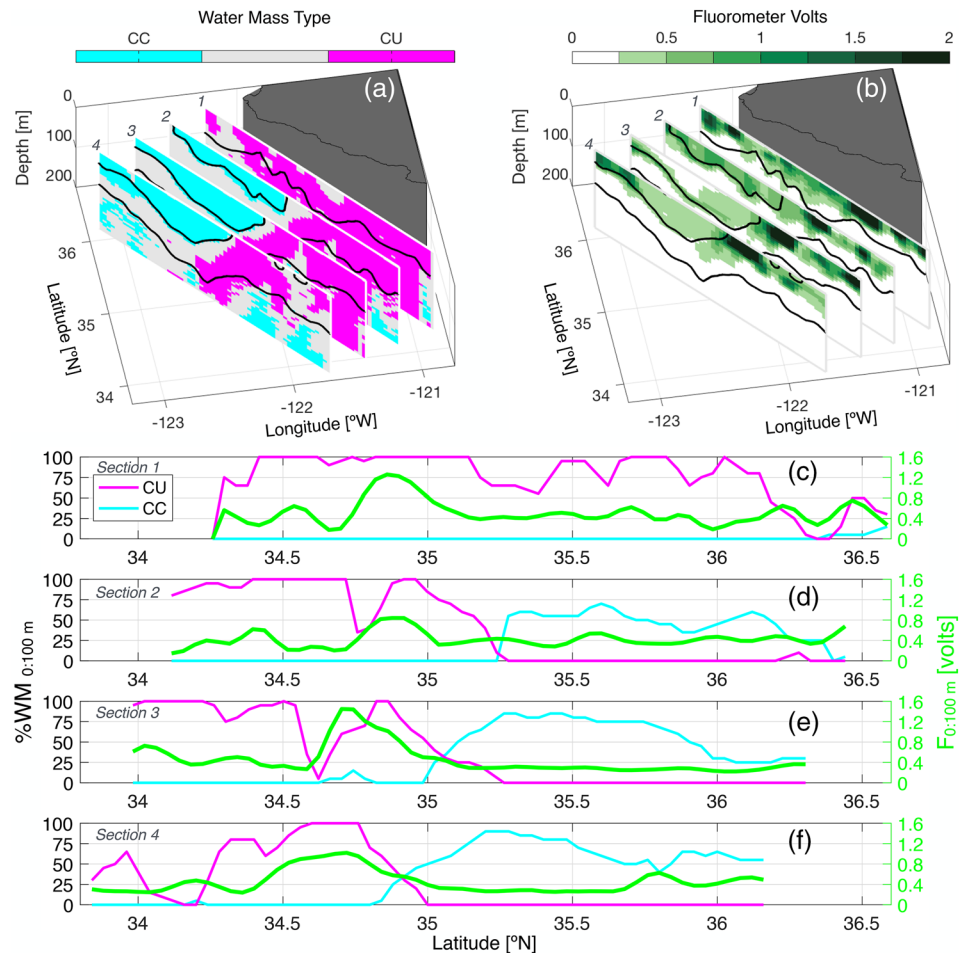


Figure 6. Three-dimensional sections of (a) water mass type and (b) fluorometer volts from SeaSoar survey 1, which occurred over June 3–6, 2017. The black contour lines in (a and b) are the 25 and 26 kg/m^3 isopycnals. Along-section properties along sections 1–4 (c–f): water mass percentage of CU (magenta) and CC (cyan) according to the left y-axis; depth-integrated fluorometer volts (green) according to the right y-axis. Percentages and depth integrals are calculated over 0–100 m.

tegrated over 0–100 m (+0.5 Sv, Figure 5a) and over 0–500 m (+1.6 Sv). Along its path, the jet may have been influenced by local upwelling, as suggested by doming of the 26–26.5 kg/m^3 isopycnals (Figure 4), and alongshore convergence (Figure 4d) within the filament. At the front, tilted isopycnals were in thermal wind balance with the offshore geostrophic velocity (Figure 4b). No such front nor consequent geostrophically balanced jet was observed during the other glider sections (Figures S2–S7). Near the surface (0–100 m), the front separated dense, salty water on the south side from light, fresh water on the north side (Figure 4a). Subsurface (200–500 m), the filament contained saltier water than its surroundings, both in an isobar and isopycnal sense (Figure 4a).

Tagged water parcels reveal distinct water mass compositions in the shallow and deep portions of the filament. Above the 25.5 kg/m^3 isopycnal, the offshore-flowing jet carried salty CU water on its south side and some fresh CC water on its north side (Figure 4a and 4b). $\% \text{CU}_{0:100}$ and $\% \text{CC}_{0:100}$ as a function of cross-filament distance (or latitude) were inversely related, and nearly monotonically decreasing and increasing, respectively (Figure 5c). South of about 35.11°N, or ~ 137.5 km along-section distance, $\% \text{CU}_{0:100}$ is greater than $\% \text{CC}_{0:100}$, up to 100% in some profiles. North of that location, $\% \text{CC}_{0:100}$ dominates, up to 70%. Below the 25.5 kg/m^3 isopycnal, the deeper portion of the filament carries almost entirely salty CU water (Figure 4a and 4b) and is flanked on both sides by onshore-flowing, fresh CC water. $\% \text{CU}_{0:500\text{m}}$ was up to 78% within the filament (Figure 5d).

SeaSoar survey 1 provides a more synoptic depiction of the three-dimensional filament structure over 3–6 June. The front is located at the steep, outcropping 25 kg/m³ isopycnal (Figure 6a). Water mass differentiation of the SeaSoar data corroborates the patterns revealed by the *Spray* glider data: salty CU water was located south of the front and fresh CC water north. The front and its associated cross-front water mass separation was present in the upper 100 m of sections 2–4 (Figures 6a, 6d–6f), where the section numbers increase with distance from shore. SeaSoar survey 1 section 4 had the closest spatial proximity to glider Lap 1, Line W (Figure 1a), which was analyzed above, though the observed SeaSoar and glider sections were separated temporally by 10–19 days. Thus, we expect SeaSoar survey 1 section 4 (Figure 6f) to be most like glider Lap 1, Line W (Figure 5c), though not identical as the filament evolved in time. SeaSoar survey 1 section 1 was closest to the coast and its water mass composition was primarily salty CU water (Figure 6a and 6c), with over half of the section 1 profiles having a %CU_{0:100} value of 80%–100%. The cross-shore variations of section 1–4 water mass compositions motivate the hypothesis that the CU water in section 1 could have been the source water for the Morro Bay filament in sections 2–4, having been upwelled near the coast and subsequently transported offshore by the filament. However, it was not the sole source, as revealed by the abutment of CU and CC water mass types at the front in sections 2–4 (Figures 6a, 6d–6f). SeaSoar survey 2 over 26–30 June did not capture a sharp front (Figure S8).

3.3. Water Mass Dependence of Biological Productivity

At the surface, the cold (south) side of the front was coincident with high Chl-*a* concentrations relative to the warm (north) side (Figures 1b and 3b). Subsurface glider-measured Chl-*a* fluorescence was maximal at the surface on the south side of the front (Figure 4c), which corresponded with the presence of CU water. The less dense, fresh CC water on the north side of the front did not support euphotic zone Chl-*a* fluorescence levels that were as high. In the CC-dominated onshore flow (Figure 4b), there was a Chl-*a* fluorescence vertical maximum centered roughly on 25 kg/m³ (Figure 4c), however, these values were about a factor of two smaller than the surface maxima in the CU-dominated offshore flow. $F_{0:100}$ had a cross-front maximum at 35.01°N, or ~125 km along-section distance (Figure 5a), where %CU_{0:100} was 90% (Figure 5c). However, the offshore volume transport integrated over 0–100 m was maximum 10 km to the north at 35.09°N, or ~135 km along-section distance (Figure 5a). The cross-front offset of $F_{0:100}$ and cross-shore transport maxima indicates there was higher Chl-*a* fluorescence just to the south of the jet core than in the core itself. Furthermore, the asymmetric $F_{0:100}$ shape (Figure 5a) indicates that Chl-*a* fluorescence levels were higher in the southern half of the filament than the northern half. The maxima of $F_{0:500}$ and offshore volume transport integrated over 0–500 m are coincident at 35.01°N, or ~125 km along-section distance, though the cross-filament distribution of $F_{0:500}$ is not symmetric, with higher values on the south side (Figure 5b). About 80% of $F_{0:500}$ was located near the surface in the upper 0–100 m, $F_{0:100}$. About a month later during the glider's second pass along Line W, the highest surface chlorophyll-*a* fluorescence values were still coincident with the presence of salty CU water (Figure S4 and S7).

A similar relationship was observed during SeaSoar survey 1 over June 3–6, 2017. In sections 2–4, $F_{0:100}$ was higher on the south, CU-dominated side of the front than the north, CC-dominated side (Figures 6a, 6d–6f), indicating higher phytoplankton concentrations within the CU water. Along sections 3–4, %CU_{0:100} gradients indicate water mass heterogeneity and coincident $F_{0:100}$ gradients suggest that, along those sections, the salty CU water type had favorable conditions for phytoplankton Chl-*a* biomass accumulation. Along section 1, nearest to the coast, there was no front (Figure 6a and 6b), nor a visible correlation between %CU_{0:100} and $F_{0:100}$ (Figure 6c). In fact, there were $F_{0:100}$ gradients and a maximum despite the relative homogeneity of CU water mass type. Therefore, the coexistence of physical and biological gradients was more prevalent offshore, suggesting that there are other factors beyond %CU_{0:100} driving the growth of phytoplankton Chl-*a* biomass growth in the coastal margin.

4. Conclusion

The CCE-LTER P1706 observations presented and analyzed here provide a high-resolution depiction of cross-filament gradients and along-filament exchange of coastal CU and offshore CC water masses. During this study, the poleward alongshore CU was present near the coast while the narrow (50–80 km width) cross-

shore Morro Bay filament was observed in mid-June via satellite, a *Spray* autonomous underwater glider, and a towed SeaSoar. A cross-filament front geostrophically balanced a strong (speeds up to 0.78 m/s), vertically sheared, surface intensified, offshore-flowing jet that transported 1.5 Sv (3.8 Sv) in its upper 100 m (500 m) from the coastal margin to the open ocean. The jet was flanked on both sides by onshore flow. Hydrographic aspects of our June 2017 Morro Bay filament were similar to those of the July 1981 and 1982 Point Arena (California) filament described by Kosro and Huyer (1986), including their maximum jet speeds (~ 80 cm/s), upper ocean seaward transports (~ 1.5 Sv), and shallow fronts acting as water mass boundaries. However, we caution against generalizing these hydrographic results to all filaments; further mesoscale studies in different locations and seasons are required to characterize filament variability.

The upper 100 m of the Morro Bay filament was a horizontal convergence zone of recently upwelled CU water and offshore CC water. It had a nearly homogeneous composition of CU water below 100 m. The biological signal (Chl-*a* fluorescence) was enhanced in the CU water, relative to the CC water. These physical and biological gradients coexisted over short (~ 10 km) spatial scales in the upper 100 m of the offshore portion of the sampled jet. These gradients were less evident at the coastal root of the filament, where the water composition was predominately CU and no sharp front existed. Cross-frontal water mass composition transitioned from 100 %CU_{0:100}/0 %CC_{0:100} to 0 %CU_{0:100}/80 %CC_{0:100} over ~ 30 km (Figure 5c). Over that same depth and horizontal distance, $F_{0:100}$ changed from roughly 0.80 to 0.25 volts, a 69% decrease (Figure 5a). By our definition, the climatological CU and CC water masses have a mean cross-shore separation of at least 80 km (Figure 2a and 2b). Furthermore, the CU and CC carry southerly Equatorial Pacific water and northerly Pacific Subarctic water, respectively, which originate many hundreds of kilometers apart alongshore, as shown numerically by Todd et al. (2012). Following upwelling, these distinct and disparate water masses were brought into close proximity to form a filament; however, it was almost exclusively the CU water that showed biological enhancement in the filament, perhaps attributable to time lags before phytoplankton production was stimulated in recently upwelled waters. In past studies, a filament jet was thought to be a boundary separating water masses and species (Hood et al., 1990). Modern high-resolution measurements allow us to zoom in to resolve small-scale gradients within the boundary itself and to consider the biological interactions occurring therein. It is clear from our analyses that dynamic, physical features such as a filament must not be assumed to be homogeneous in terms of their source waters—with consequent ecological dynamics.

This water mass decomposition analysis was enabled by the complementary use of high-resolution historical data (CUGN climatology) and process study data (P1706 observations), where the statistical view from the climatology informed the event view of the experiment. In creating the CUGN climatology, Rudnick et al. (2017) aimed to provide a data product that could place in context other regional measurements in the southern to central CCS. It is applied for that purpose here, with water mass definitions derived from the CUGN climatology's mean cross-shore structure of alongshore currents and θ -S properties used to contextualize cross-shore transport by a filament at much shorter spatiotemporal scales. In previous studies, including the CTZ experiments, water mass definitions were derived from the same filament process studies to which they were applied (de Verneil et al., 2019; Huyer et al., 1991; Kosro & Huyer, 1986; Strub et al., 1991). Today we have access to independent, historical, high resolution data products of the CCS region that provide a robust baseline for contextualizing synoptic measurements.

In this work, we conclude that in June 2017 the Morro Bay filament was effective at transporting coastal CU water, phytoplankton Chl-*a*, and probably other planktonic organisms from the coastal margin to the open ocean, bringing recently upwelled water with a high biological signature into an otherwise depleted (oligotrophic) environment. However, there are many remaining research questions about the influence of filaments on the gradients and cross-shore fluxes of biogeochemical variables such as oxygen, nutrients (nitrate, phosphate, silicic acid), and particulate organic carbon (Barth et al., 2002). Some biogeochemical consequences of the Morro Bay filament are being assessed in a Lagrangian framework by other CCE-LTER team members; to understand other consequences would require higher-resolution biogeochemical measurements. The nutrient landscape of the CCS is complex (Stukel & Barbeau, 2020), with filaments stirring it even further. Collocated measurements from a common platform would enable the assessment of physical and biogeochemical gradient relationships and the calculation of biogeochemical budgets within filaments. The development and integration of reliable biogeochemical sensors onto autonomous platforms is ongoing (Chai et al., 2020).

Data Availability Statement

The merged California Current satellite data product (<http://spg-satdata.ucsd.edu/>) and CUGN climatology (<http://spraydata.ucsd.edu/climCUGN/>) are available online.

Acknowledgments

We thank all the participants in the CCE-LTER P1706 process cruise for contributing to the measurements analyzed here, and especially Carl Mattson for SeaSoar operations. We gratefully acknowledge Jeff Sherman, Dan Rudnick, and the SIO Instrument Development Group for *Spray* glider operations, the Franks Lab group members for their constructive feedback on analysis in this study, and Mati Kahru for providing satellite data. This work was supported by grants to the *California Current Ecosystem* LTER site by the US National Science Foundation.

References

- Barth, J. A., Cowles, T. J., Kosro, P. M., Shearman, R. K., Huyer, A., & Smith, R. L. (2002). Injection of carbon from the shelf to offshore beneath the euphotic zone in the California Current. *Journal of Geophysical Research*, *107*(C6), 3057. <https://doi.org/10.1029/2001JC000956>
- Barth, J. A., Pierce, S. D., & Cowles, T. J. (2005). Mesoscale structure and its seasonal evolution in the northern California Current System. *Deep Sea Research Part II: Topical Studies in Oceanography*, *52*, 5–28.
- Bograd, S. J., Schroeder, I. D., & Jacox, M. G. (2019). A water mass history of the Southern California Current System. *Geophysical Research Letters*, *46*, 6690–6698. <https://doi.org/10.1029/2019GL082685>
- Brink, K. H., & Cowles, T. J. (1991). The coastal transition zone program. *Journal of Geophysical Research*, *96*, 14637–14647.
- Centurioni, L. R., Ohlmann, J. C., & Niiler, P. P. (2008). Permanent meanders in the California Current System. *Journal of Physical Oceanography*, *38*, 1690–1710.
- Chai, F., Johnson, K. S., Claustre, H., Xing, X., Wang, Y., Boss, E., et al. (2020). Monitoring ocean biogeochemistry with autonomous platforms. *Nature Reviews Earth and Environment*, *1*, 315–326.
- Chereskin, T. K. (1995). Direct evidence for an Ekman Balance in the California Current. *Journal of Geophysical Research*, *100*, 18261–18269.
- Chereskin, T. K., Morris, M. Y., Niiler, P. P., Kosro, P. M., Smith, R. L., Ramp, S. R., et al. (2000). Spatial and temporal characteristics of the mesoscale circulation of the California Current from eddy-resolving moored and shipboard measurements. *Journal of Geophysical Research*, *105*, 1245–1269.
- Davis, R. E. (1985). Drifter observations of coastal surface currents during code—The method and descriptive view. *Journal of Geophysical Research*, *90*, 4741–4755.
- Davis, R. E. (2010). On the coastal-upwelling overturning cell. *Journal of Marine Research*, *68*, 369–385.
- de Verneil, A., Franks, P. J. S., & Ohman, M. D. (2019). Frontogenesis and the creation of fine-scale vertical phytoplankton structure. *Journal of Geophysical Research: Oceans*, *124*, 1509–1523. <https://doi.org/10.1029/2018JC014645>
- Ferrari, R., & Rudnick, D. L. (2000). Thermohaline variability in the upper ocean. *Journal of Geophysical Research*, *105*, 16857–16883.
- Gomez-Valdivia, F., Pares-Sierra, A., & Flores-Morales, A. L. (2017). Semiannual variability of the California Undercurrent along the Southern California Current System: A tropical generated phenomenon. *Journal of Geophysical Research: Oceans*, *122*, 1574–1589.
- Hickey, B. M. (1979). The California Current System—Hypotheses and facts. *Progress in Oceanography*, *8*, 191–279.
- Hickey, B. M., & Banas, N. S. (2003). Oceanography of the U. S. Pacific Northwest Coastal Ocean and estuaries with application to coastal ecology. *Estuaries*, *26*, 1010–1031.
- Hood, R. R., Abbott, M. R., & Huyer, A. (1991). Phytoplankton and photosynthetic light response in the coastal transition zone off Northern California in June 1987. *Journal of Geophysical Research*, *96*, 14769–14780.
- Hood, R. R., Abbott, M. R., Huyer, A., & Kosro, P. M. (1990). Surface patterns in temperature, flow, phytoplankton biomass, and species composition in the coastal transition zone off Northern California. *Journal of Geophysical Research*, *95*, 18081–18094.
- Huyer, A., Kosro, P. M., Fleischbein, J., Ramp, S. R., Stanton, T., Washburn, L., et al. (1991). Currents and water masses of the coastal transition zone off Northern California, June to August 1988. *Journal of Geophysical Research*, *96*, 14809–14831.
- Jacox, M. G., Edwards, C. A., Hazen, E. L., & Bograd, S. J. (2018). Coastal Upwelling Revisited: Ekman, Bakun, and Improved Upwelling Indices for the US West Coast. *Journal of Geophysical Research: Oceans*, *123*, 7332–7350. <https://doi.org/10.1029/2018JC014187>
- Keister, J. E., Cowles, T. J., Peterson, W. T., & Morgan, C. A. (2009). Do upwelling filaments result in predictable biological distributions in coastal upwelling ecosystems? *Progress in Oceanography*, *83*, 303–313.
- Keister, J. E., Peterson, W. T., & Pierce, S. D. (2009). Zooplankton distribution and cross-shelf transfer of carbon in an area of complex mesoscale circulation in the northern California Current. *Deep Sea Research Part I*, *56*, 212–231.
- Kenitz, K. M., Visser, A. W., Ohman, M. D., Landry, M. R., & Andersen, K. H. (2019). Community trait distribution across environmental gradients. *Ecosystems*, *22*, 968–980.
- Kosro, P. M., & Huyer, A. (1986). Ctd and velocity surveys of seaward jets off Northern California, July 1981 and 1982. *Journal of Geophysical Research*, *91*, 7680–7690.
- Lynn, R. J., & Simpson, J. J. (1987). The California Current System—The seasonal variability of its physical characteristics. *Journal of Geophysical Research*, *92*, 12947–&.
- Mackas, D. L., Washburn, L., & Smith, S. L. (1991). Zooplankton community pattern associated with a California Current cold filament. *Journal of Geophysical Research*, *96*, 14781–14797.
- McClatchie, Sam, Cowen, Robert, Nieto, Karen, Greer, Adam, Luo, Jessica Y., Guigand, Cedric, et al. (2012). Resolution of fine biological structure including small narcomedusae across a front in the Southern California Bight. *Journal of Geophysical Research: Oceans*, *117*, (C4), n/a–n/a. <http://dx.doi.org/10.1029/2011jc007565>.
- Ohman, M. D., Barbeau, K., Franks, P. J. S., Goericke, R., Landry, M. R., & Miller, A. J. (2013). Ecological transitions in a coastal upwelling ecosystem. *Oceanography*, *26*, 210–219.
- Pierce, S. D., Smith, R. L., Kosro, P. M., Barth, J. A., & Wilson, C. D. (2000). Continuity of the poleward undercurrent along the eastern boundary of the mid-latitude north Pacific. *Deep Sea Research Part II*, *47*, 811–829.
- Pollard, R. (1986). Frontal surveys with a towed profiling conductivity temperature depth measurement package (SeaSoar). *Nature*, *323*, 433–435.
- Powell, J. R., & Ohman, M. D. (2015). Covariability of zooplankton gradients with glider-detected density fronts in the Southern California Current System. *Deep Sea Research Part II*, *112*, 79–90.
- Rudnick, D. L., Sherman, J. T., & Wu, A. P. (2018). Depth-average velocity from spray underwater gliders. *Journal of Atmospheric and Oceanic Technology*, *35*, 1665–1673.
- Rudnick, D. L., Zaba, K. D., Todd, R. E., & Davis, R. E. (2017). A climatology of the California Current System from a network of underwater gliders. *Progress in Oceanography*, *154*, 64–106.
- Rykaczewski, R. R., & Checkley, D. M. (2008). Influence of ocean winds on the pelagic ecosystem in upwelling regions. *Proceedings of the National Academy of Sciences of the United States of America*, *105*, 1965–1970.

- Sherman, J., Davis, R. E., Owens, W. B., & Valdes, J. (2001). The autonomous underwater glider spray. *IEEE Journal of Oceanic Engineering*, *26*, 437–446.
- Strub, P. T., Kosro, P. M., & Huyer, A. (1991). The nature of the cold filaments in the California Current System. *Journal of Geophysical Research*, *96*, 14743–14768.
- Stukel, M. R., & Barbeau, K. A. (2020). Investigating the nutrient landscape in a coastal upwelling region and its relationship to the biological carbon pump. *Geophysical Research Letters*, *47*(6), e2020GL087351. <https://doi.org/10.1029/2020GL087351>
- Thomson, R. E., & Krassovski, M. V. (2010). Poleward reach of the California Undercurrent extension. *Journal of Geophysical Research*, *115*, C09027. <https://doi.org/10.1029/2010JC006280>
- Todd, R. E., Rudnick, D. L., Mazloff, M. R., Cornuelle, B. D., & Davis, R. E. (2012). Thermohaline structure in the California Current System: Observations and modeling of spice variance. *Journal of Geophysical Research*, *117*, C02008. <https://doi.org/10.1029/2011JC007589>
- Zaba, K. D. (2020). Volume and heat budgets in the coastal California Current System: Means, annual cycles and interannual anomalies of 2014-2016. *Journal of Physical Oceanography*, *50*, 1435–1453.
- Zaba, K. D., Rudnick, D. L., Cornuelle, B. D., Gopalakrishnan, G., & Mazloff, M. R. (2018). Annual and interannual variability in the California Current System: Comparison of an ocean state estimate with a network of underwater gliders. *Journal of Physical Oceanography*, *48*, 2965–2988.

1
2
3
4
5
6
7
8
9
10
11
12
13
14
15
16
17
18
19
20
21
22
23

Supporting Information

The California Undercurrent as a source of upwelled waters in a coastal filament

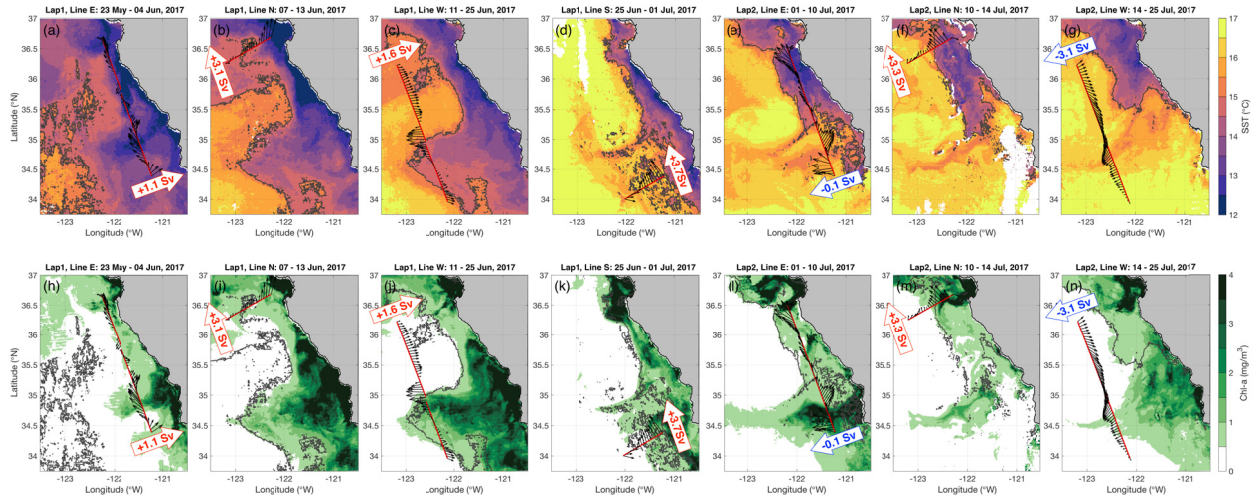
Authors: Katherine D. Zaba^{1*}, Peter J. S. Franks¹, Mark D. Ohman¹

Affiliations:

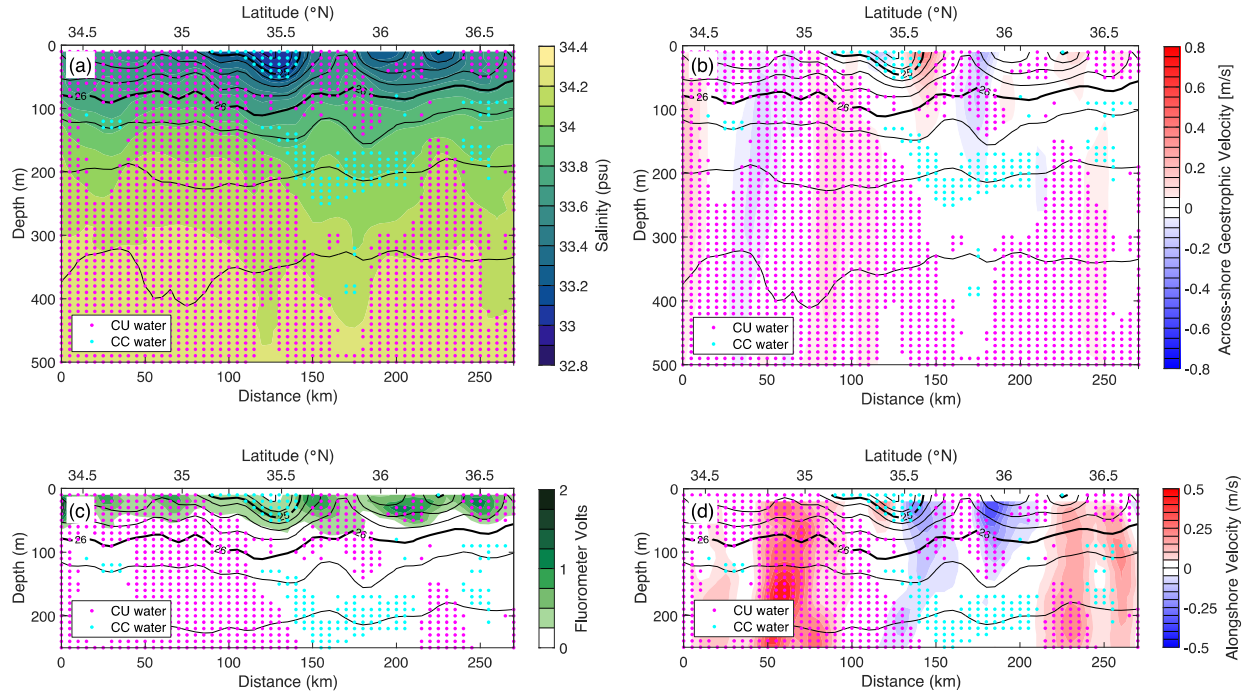
¹Scripps Institution of Oceanography, La Jolla, CA 92093-0213, USA.

*To whom correspondence should be addressed. E-mail: kzaba@ucsd.edu

24
25
26
27
28

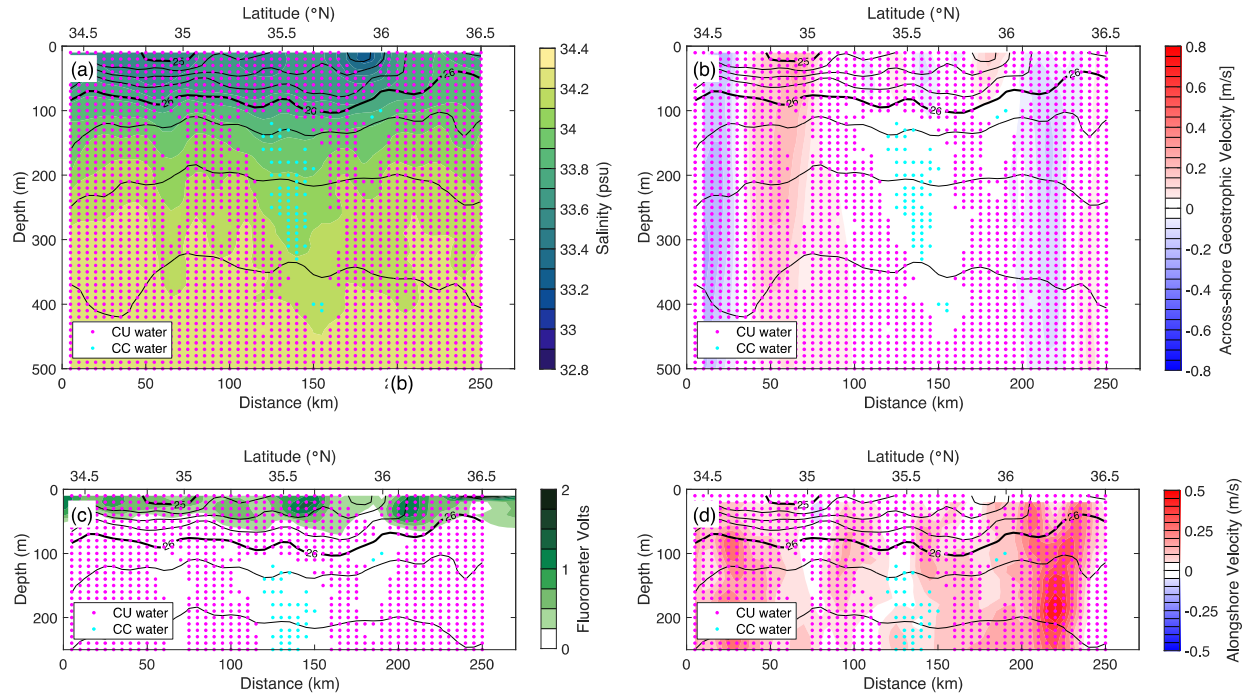


29
30 **Figure S1:** The evolution of physical and biological conditions, illustrated separately for each
31 glider section: (a,h) Lap 1, Line E, (b,i) Lap 1, Line N, (c,j) Lap1, Line W, (d,k) Lap 1, Line S,
32 (e,l) Lap 2, Line E, (f,m) Lap 2, Line N, and (g,n) Lap 2, Line S. Panels (a-g) (top row) show
33 sea surface temperature, and panels (h-n) (bottom row) surface chlorophyll-*a* concentrations,
34 time-averaged over the duration of each glider section. All panels show the 15°C surface
35 isotherm and glider-derived objectively mapped 0-500 m depth-averaged velocities (thin black
36 arrows). The 0-500m integrated cross-section volume transports are labeled in the thick block
37 arrows, where positive transports (red) are defined as onshore and poleward and negative (blue)
38 as offshore and equatorward.



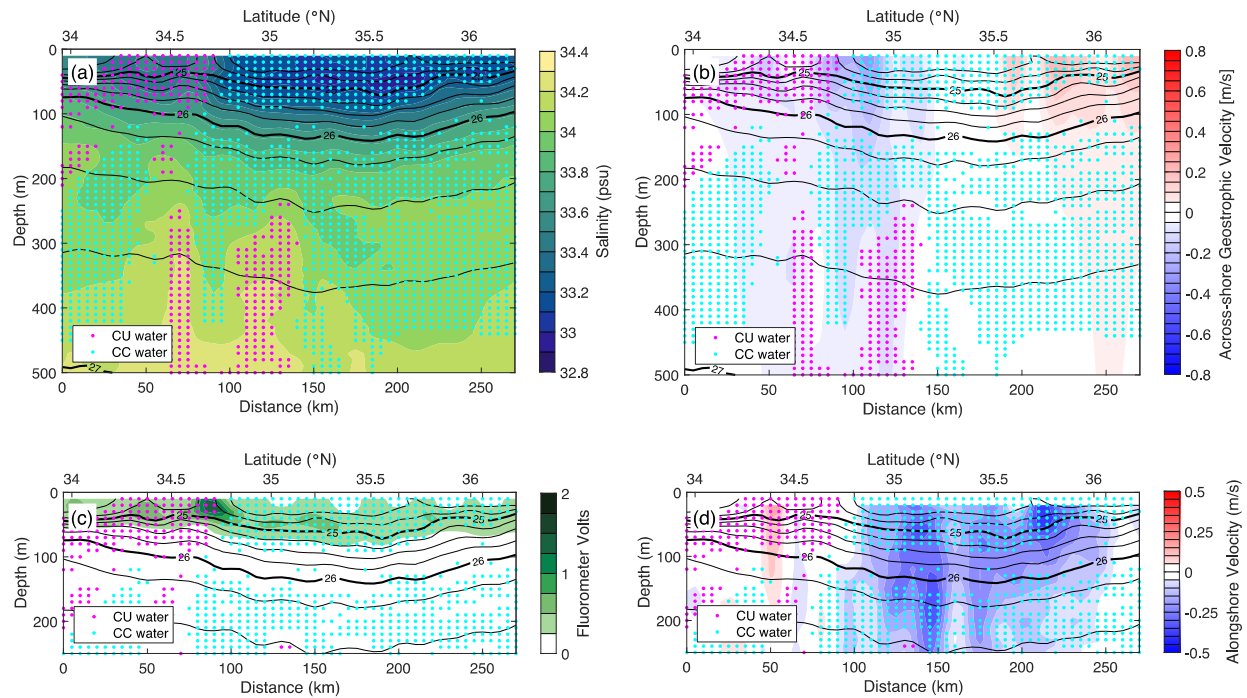
39
 40 **Figure S2:** Depth-dependent sections along glider lap 1, line E of: (a) salinity, (b) cross-shore
 41 geostrophic velocity, (c) fluorometer volts, and (d) ADP-measured alongshore. In the
 42 geostrophic velocity colormap (b), blue background shading represents offshore flow and red
 43 onshore. In the alongshore velocity colormap (d), blue background shading represents
 44 equatorward flow and red poleward. The black lines are isopycnals. The magenta dots represent
 45 CU water parcels and the cyan dots CC water parcels.

46



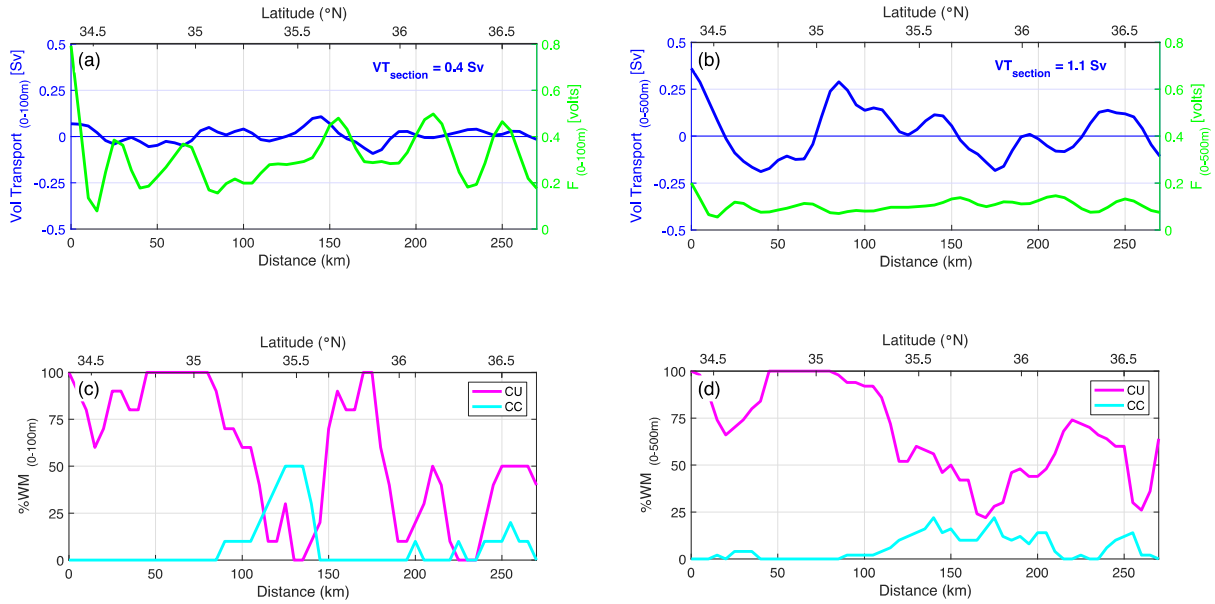
47
 48 **Figure S3:** Depth-dependent sections along glider lap 2, line E of: (a) salinity, (b) cross-shore
 49 geostrophic velocity, (c) fluorometer volts, and (d) ADP-measured alongshore. In the
 50 geostrophic velocity colormap (b), blue background shading represents offshore flow and red
 51 onshore. In the alongshore velocity colormap (d), blue background shading represents
 52 equatorward flow and red poleward. The black lines are isopycnals. The magenta dots represent
 53 CU water parcels and the cyan dots CC water parcels.

54



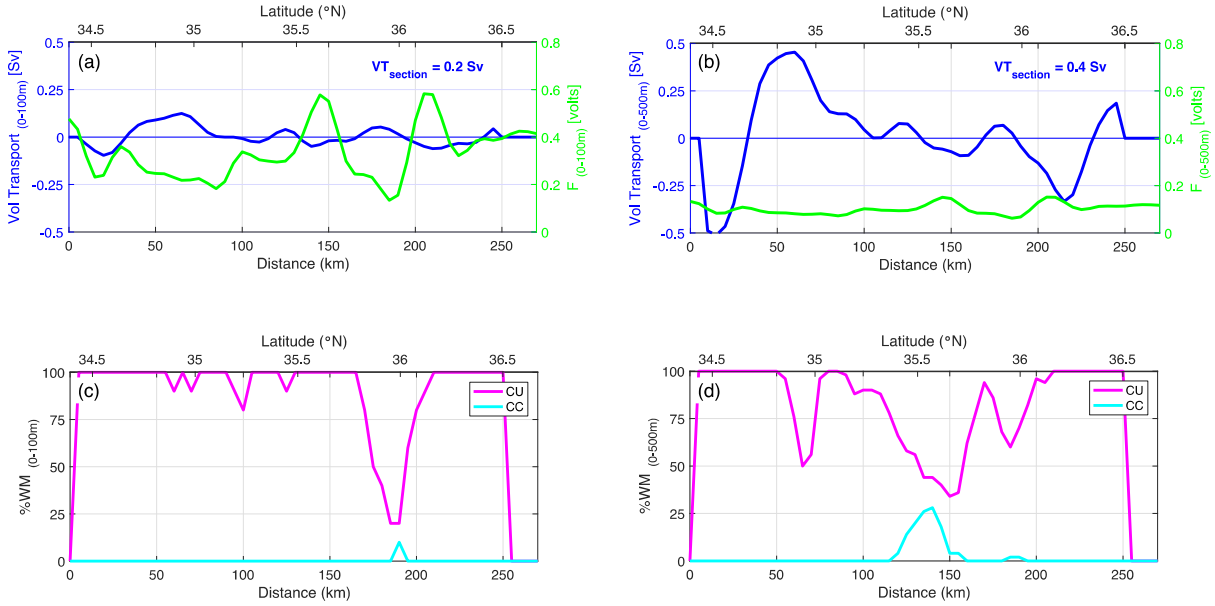
55
 56 **Figure S4:** Depth-dependent sections along glider lap 2, line W of: (a) salinity, (b) cross-shore
 57 geostrophic velocity, (c) fluorometer volts, and (d) ADP-measured alongshore. In the
 58 geostrophic velocity colormap (b), blue background shading represents offshore flow and red
 59 onshore. In the alongshore velocity colormap (d), blue background shading represents
 60 equatorward flow and red poleward. The black lines are isopycnals. The magenta dots represent
 61 CU water parcels and the cyan dots CC water parcels.

62
 63



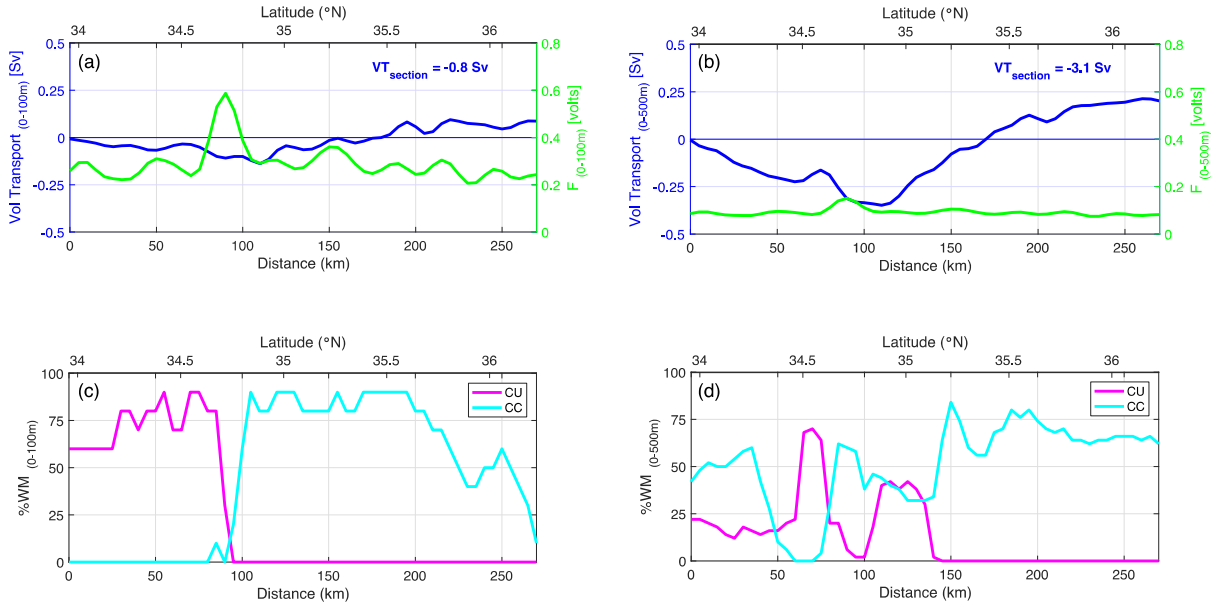
64
 65 **Figure S5:** Glider-measured properties along lap 1, line E. (a,b) Depth-integrated cross-shore
 66 volume transport (blue) and depth-integrated fluorometer volts. (c,d) Water mass percentage of
 67 CU (magenta) and CC (cyan). Depth integrals and percentages are calculated over (a,c) 0-100 m
 68 and (b,d) 0-500 m. The cross-shore volume transport integrated over the entire section (VT_{section})
 69 is reported in blue text in (a,b).

70
 71
 72
 73

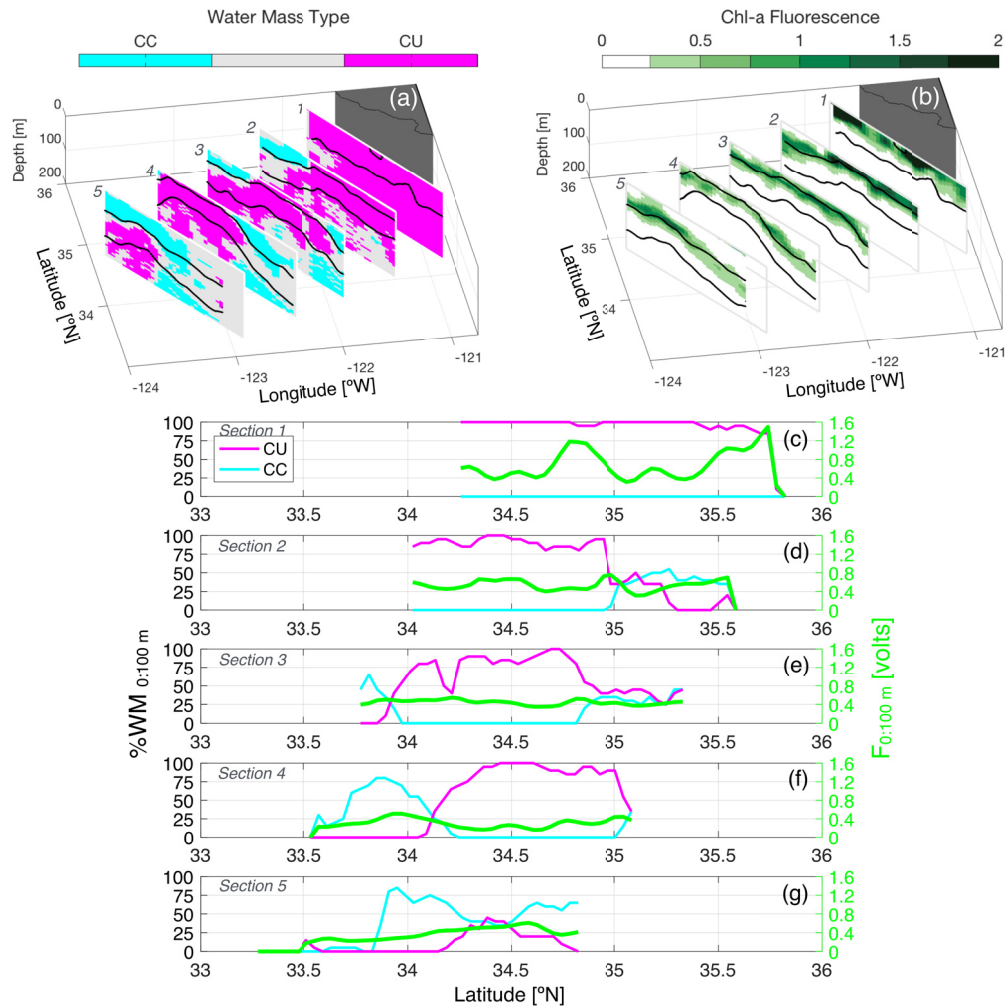


74
 75 **Figure S6:** Glider-measured properties along lap 2, line E. (a,b) Depth-integrated cross-shore
 76 volume transport (blue) and depth-integrated fluorometer volts. (c,d) Water mass percentage of
 77 CU (magenta) and CC (cyan). Depth integrals and percentages are calculated over (a,c) 0-100 m
 78 and (b,d) 0-500 m. The cross-shore volume transport integrated over the entire section (VT_{section})
 79 is reported in blue text in (a,b).

80
 81
 82
 83



84
 85 **Figure S7:** Glider-measured properties along lap 2, line W. (a,b) Depth-integrated cross-shore
 86 volume transport (blue) and depth-integrated fluorometer volts. (c,d) Water mass percentage of
 87 CU (magenta) and CC (cyan). Depth integrals and percentages are calculated over (a,c) 0-100 m
 88 and (b,d) 0-500 m. The cross-shore volume transport integrated over the entire section (VT_{section})
 89 is reported in blue text in (a,b).



91
 92 **Figure S8:** Three-dimensional sections of (a) water mass type and (b) fluorometer volts from
 93 SeaSoar survey 2, which occurred over 26-30 June 2017. The black contour lines in (a,b) are the
 94 25 and 26 kg/m^3 isopycnals. Along-section properties along sections 1-5 (c-f): water mass
 95 percentage of CU (magenta) and CC (cyan) according to the left y-axis; depth-integrated
 96 fluorometer volts (green) according to the right y-axis. Percentages and depth integrals are
 97 calculated over 0 - 100 m.